Static Behaviour and Classification of Shear-Thinning Droplets on Inclined Hydrophobic Substrates

Rohit[a], Syed Ahsan Haider[a], Abhishek Raj[a,*]

[a]*Department of Mechanical Engineering, Indian Institute of Technology Patna, India*
[*]*Corresponding Author, araj@iitp.ac.in*

Abstract

This study presents a comprehensive investigation into the static behaviour and shape evolution of shear-thinning liquid droplets compared to Newtonian droplets when gently deposited on a rigid substrate. The manner of droplet placement significantly influences the resulting equilibrium shape, with these effects becoming more pronounced when the droplet is placed on an inclined surface due to the action of gravitational tangential forces. A mathematical analysis highlights that the shear stress within a hemispherical droplet varies along its height when placed on an inclined substrate, leading to asymmetrical deformation and resulting in macroscopic contact angle hysteresis (CAH). Experimental observations reveal that this deformation is notably different for shear-thinning liquids compared to Newtonian ones. Shear-thinning droplets demonstrate a more compact and deformable shape, exhibiting up to 20.12% shorter base length (L) and 12.5% greater height (H) than Newtonian droplets. These geometric differences contribute to a significantly higher CAH, up to 115.68% greater, which enhances the droplet's ability to resist motion and increases its retention on the surface. Retained volumes of shear-thinning droplets were found to be 50%–350% greater than those of their Newtonian counterparts on the inclined Polydimethylsiloxane (PDMS)-coated glass substrate. To quantify these differences, a novel dimensionless number, the Droplet Rheology Classifier (DRC) number ($DRC = H/L\ (Cos\theta_R - Cos\theta_F)$), is introduced, capturing the combined effects of droplet geometry and macroscopic contact angle hysteresis. The DRC no is found to successfully classify sessile droplets placed on inclined substrates into shear-thinning and Newtonian populations. Building upon these distinct geometrical and wetting characteristics, this study demonstrates a novel classification approach using Support Vector Machine (SVM) modelling. By training the SVM on geometric features extracted from side-view images of droplets placed on an inclined surface, the model effectively differentiates between Newtonian and shear-thinning fluids with 95% classification accuracy. This image-based, non-invasive technique offers promising potential for fluid classification in biomedical diagnostics, particularly for detecting diseases where changes in the rheology of biological fluids ($e.g.$, blood, saliva, sputum) serve as key indicators of pathological conditions.

Keywords: *Shear-thinning fluids, Droplet deformation, Contact angle hysteresis, Inclined surface wetting, Inclined droplet morphology, Machine learning classification*

Nomenclature

ρ	Density of the droplet (kg/m^3)
σ	Surface tension (mN/m)
μ_∞	Viscosity of liquid at high shear rate ($Pa.s$)
δ	Inclination angle of substrate (°)
θ_F, θ_R	Macroscopic contact angles at the front (downslope) and rear (upslope) of the droplet, respectively (°)
CAH	$cos\ \theta_R - cos\ \theta_F$ [Dimensionless]
K_R	Droplet contour factor for receding side [dimensionless]
$\sigma_{la}, \sigma_{ls}, \sigma_{as}$	Interfacial tension between liquid-air, liquid–substrate and air-substrate respectively (N/m)
N	power-law index
λ	relaxation time scale (s)

1. Introduction

The behaviour of liquid droplets on solid surfaces continues to be a topic of significant scientific and practical importance, owing to its critical role in various natural phenomena and industrial applications. Processes such as inkjet printing[1], spray coating [2], agrochemical delivery[3], micro-optics fabrication [4], pharmaceutical deposition[5], and fire suppression[6] depend heavily on the ability to accurately predict and control droplet surface interactions[7,8]. These interactions are governed by a complex interplay of interfacial forces, including surface tension, adhesion, gravity, and viscous effects [9–11]. A fundamental understanding of droplet statics, particularly parameters such as droplet shape, contact angle, and retention force, provides essential insights into surface wettability and the performance of materials under practical operating conditions.

Previous research in this domain has predominantly focused on Newtonian liquids, whose constant viscosity offers a simplified framework for both theoretical modelling and experimental investigation. Foundational studies have systematically examined the static and dynamic behaviours of Newtonian droplets on smooth, chemically homogeneous, and rigid substrates [8,12]. Seminal contributions by Extrand and colleagues, among others, established quantitative relationships between contact angle hysteresis (CAH), droplet geometry, and the retentive force experienced on inclined surfaces[13–15]. In parallel, Furmidge provided an analytical expression linking CAH to the minimum force required to initiate droplet motion, thereby laying the foundation for understanding droplet adhesion phenomena[16]. These investigations collectively revealed that droplet retention is significantly influenced by factors such as droplet volume, geometry, surface energy, and the angle of substrate inclination.

However, in practical applications, many functional fluids employed across diverse industries exhibit non-Newtonian behaviour [17,18], wherein viscosity varies with the applied shear rate [17]. Among these, shear-thinning fluids characterised by a reduction in viscosity with increasing shear are particularly prevalent. Examples include polymer solutions, biological fluids such as blood and mucus, personal care formulations, food emulsions, and industrial coatings[19,20]. The shear-dependent resistance in these fluids typically arises from internal microstructural changes, such as polymer chain entanglement or particle alignment, which adds complexity to their interaction with solid surfaces [21,22]. While recent simulation-based studies, such as those involving magnetorheological fluids, have started probing such complexities in wetting and spreading dynamics[23], the impact of non-Newtonian rheology, on static droplet behaviour of shear thinning liquid on inclined substrates remains comparatively underexplored in a systematic manner.
The behaviour of a droplet on an inclined surface differs markedly from that on a horizontal substrate due to the presence of a gravitational force component acting parallel to the plane. This additional force competes with the adhesive forces at the liquid-solid interface, thereby affecting the droplet's equilibrium shape, retention threshold, and likelihood of motion[16,24–26]. For Newtonian fluids, this force balance has been effectively captured through classical theoretical models. However, in the case of shear-thinning fluids, the scenario becomes considerably more complex. The effective viscosity within such droplets is not spatially uniform but instead varies dynamically in response to internal shear gradients induced by gravity and capillary forces. This rheological non-uniformity can lead to distinctive droplet morphologies, modified contact angle hysteresis (CAH), and altered retention behaviour, even under nominally static conditions.
Previous studies comparing the spreading behaviour of Newtonian and shear-thinning droplets on rigid substrates have shown notable differences. For instance, An et al. [27] investigated the impact dynamics of shear-thinning droplets on solid surfaces, with a primary focus on their spreading and retraction behaviour. Through experimental observations, they demonstrated distinct differences in their dynamic responses due to the viscosity of both Newtonian and non-Newtonian fluids. Starov et al.[28] developed a mathematical model to describe the spreading behaviour of non-Newtonian liquids on solid, rigid substrates. Their findings revealed that shear-thinning droplets maintain a greater height during spreading compared to Newtonian droplets. Further, Researchers have [29,30] investigated the spreading dynamics of shear-thinning droplets with varying power-law indices. It has been established that as the degree of shear thinning increases, the rate of spreading decreases, highlighting the influence of rheological properties on droplet behaviour. Further, Varagnolo *et al*.,[31] examined the steady state motion of Shear thinning and Newtonian liquid over a rigid substrate considering the steady state viscosity of the

Shear thinning liquids and found that the Shear thinning liquid was deviated from the linear trend of relationship between Bond number and capillary number in case of Newtonian liquids.

Despite the technological significance of non-Newtonian droplets, comparative studies examining Newtonian and shear-thinning droplets under identical conditions on inclined, rigid surfaces remain limited (refer to Table 1). In particular, there is a notable scarcity of investigations that quantitatively assess the static geometrical differences arising solely from rheological variations. Gaining insight into these differences is essential for applications where fluid identification or classification must rely exclusively on visual or geometric characteristics. Such scenarios are common in quality control of complex formulations, automated fluid recognition in microfluidic systems, and diagnostic imaging of biological samples.

To address this gap, the present study systematically investigates the static behaviour of shear-thinning droplets on inclined Polydimethylsiloxane (PDMS)-coated glass substrates, a model rigid surface with well-defined hydrophobic characteristics. The PDMS coating ensures consistent wettability across experiments while minimising variability due to surface roughness or chemical heterogeneity. The shear-thinning droplets used in this study are aqueous solutions of Xanthan Gum. For comparison, Newtonian liquids with viscosities matching the zero-shear (μ_0) and infinite-shear (μ_∞) viscosities of the Xanthan gum solution are used to isolate the effects of rheology from other fluid properties such as surface tension or density.

A detailed analysis of key static parameters such as macroscopic contact angle hysteresis (CAH), droplet base length, height, and volume was performed using high-resolution side-view imaging. These geometrical and interfacial parameters provide quantifiable indicators of droplet deformation and wetting behaviour on inclined surfaces. As outlined above, the objective is to provide a quantitative understanding of how fluid rheology influences droplet shape, wetting behaviour, and retention on inclined surfaces. These differences in droplet geometry, particularly in base length, height, and macroscopic CAH, serve as key indicators of the underlying fluid type and are further utilised to classify the liquids as Newtonian or shear-thinning.

To unify the geometrical and wetting characteristics into a single dimensionless parameter, a Droplet Rheology Classifier (DRC) number is introduced. This metric captures the combined effects of droplet aspect ratio and macroscopic contact angle hysteresis, enabling effective differentiation between Newtonian and shear-thinning fluids based on their equilibrium shape and interfacial behaviour on inclined surfaces. In parallel, a Support Vector Machine (SVM) [19,20] model is developed and trained using the same geometrical features to classify droplets purely from their visual and morphological attributes. As shown in Fig. 1(b), both the DRC and SVM frameworks offer complementary approaches for fluid classification. In the SVM classification in Fig 1(b), the two axes x_1 and x_2 represent optimized feature dimensions in the SVM classification space, derived from combinations of input parameters to best separate the data classes. This method holds significant potential for biomedical diagnostics, as changes in the rheology of biological fluids are often indicative of disease. For example, in sickle cell anaemia [32,33], the altered shape of red blood cells leads to increased blood viscosity and impaired flow; in Sjögren's syndrome[34], decreased saliva production results in thicker, more viscous saliva and in cystic fibrosis, sputum becomes abnormally sticky, hindering lung function[35]. By identifying such rheological variations, the proposed technique provides a powerful diagnostic tool for early detection and disease monitoring.

Table 1: Previous studies in the literature

Author	Substrate	Fluid Rheology	Remarks
Extrand and Gent (1990)[15]	Rigid	Newtonian	Studied the effect of droplet geometry on retentive force
Extrand and Kumagai (1994)[14]	Rigid	Newtonian	Studied the Influence of surface and liquid properties over macroscopic CAH, droplet shape and droplet retention.

E.B. Dussan V. (1985)[36]	Rigid	Newtonian	Investigated the conditions for the onset of droplet motion on an inclined plane and aimed to predict its behaviour.
Berejnov and Throneo et al. (2007)[37]	Rigid	Newtonian	Contact line depinning leading to translational motion of droplet and Critical volume of statically pinned drop
ElSherbini and Jacobi (2006)[12]	Rigid	Newtonian	Developed the two-circle method to approximate droplet shape and proposed a general relationship between advancing and receding contact angles.
G. Ahmed et al. (2013)[38]	Rigid	non-Newtonian	A mathematical model describing the spreading and sliding behaviour of a power-law fluid, highlighting the influence of varying parameters.
Starov, V. M., *et al.* (2003)[28]	Rigid	non- Newtonian	Shear-thinning liquids show slower spreading and hence a higher height

Thus, the main novelties and scientific advancements of the current work are as follows:

- Established a direct link between shear stress variation along droplet height and internal deformation, especially in shear-thinning fluids under inclined conditions.
- Provided experimental evidence of progressive internal deformation with increasing height, a behaviour unique to shear-thinning fluids.
- Identified a Bond number (ratio of gravitational to capillary force given by, $Bo = \rho g R^2/\gamma$, where R is the droplet radius and γ is the surface tension of the liquid) threshold (>0.056) beyond which deformation becomes significant, offering a scale-independent criterion for droplet behaviour.
- Observed that shear-thinning droplets show greater height, smaller base contact length, and significantly higher retentive forces compared to Newtonian fluids.
- The distinction between Newtonian and shear-thinning droplets is effectively captured by the Droplet Rheology Classifier (DRC) number, which increases notably with higher inclination angles.
- Employed Support Vector Machine (SVM) classification to distinguish droplet types and behaviours based on shape, deformation metrics, and macroscopic CAH, providing a robust, data-driven approach to droplet analysis.

The paper is structured to ensure a clear and coherent progression of the research. Section 2 outlines the experimental and methodological framework: Section 2.1 describes the preparation and characterization of shear-thinning and Newtonian liquids; Section 2.2 details the experimental setup and procedures; Section 2.3 presents the computational approach for droplet classification using Support Vector Machine (SVM); and Section 2.4 explains the statistical methods used for data analysis.
Section 3 introduces a mathematical model describing the variation of shear stress along the height of a static droplet on an inclined substrate, providing theoretical support for the experimental observations.
Section 4 presents the results and discussion, organized into clearly defined subsections: Section 4.1 investigates the effect of shear stress on droplet deformation; Section 4.2 analyses the influence of droplet placement on its equilibrium shape; Section 4.3 compares the geometrical features of shear-thinning and Newtonian droplets; Section 4.4 explores the retention behaviour of both liquid types; and Section 4.5 demonstrates the effectiveness

of SVM-based classification of static droplets. Finally, Section 5 summarises the key findings and highlights the novel contributions of this study.

2. Materials and Methods

2.1 Preparation and characterization of the shear-thinning and Newtonian fluids

A 0.052% w/w xanthan gum (XG) solution in deionized water was used as a shear-thinning fluid with negligible viscoelasticity [39,40]. Two Newtonian glycerol-water solutions (40% and 86.7% w/w) were prepared to match the low-shear (μ_0) and high-shear (μ_∞) viscosities of the XG solution. Liquid properties are summarised in Table 2. Contact angle measurements on the PDMS-coated glass (S_{PCG}) substrate confirmed similar wettability across all liquids, as shown in Fig. S1 (Supplementary Information). Detailed preparation protocols are also provided in the Supplementary Information. From now onwards in this paper, we will address shear thinning liquid as "shear thinning (XG-1), Newtonian liquid consisting of 40% w/w aqueous glycerol solution as "Newtonian (μ_∞)" and Newtonian liquid consisting of 87% w/w aqueous glycerol solution as "Newtonian (μ_0)". This nomenclature is also highlighted in Table 2.

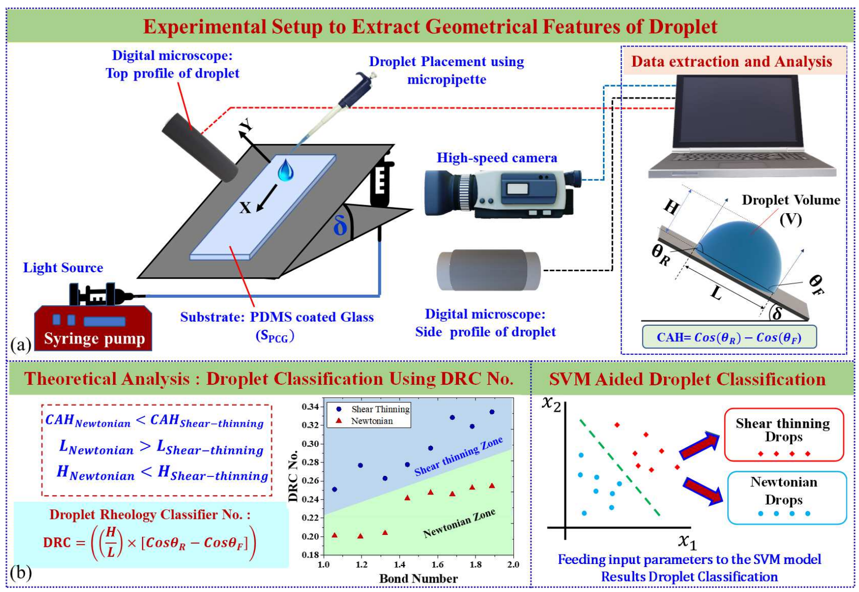

Fig. 1: Experimental setup and droplet classification framework. **(a)** Setup for capturing droplet geometry on inclined PDMS-coated glass using high-speed and digital microscopy. **(b)** Theoretical and machine learning-based classification of Newtonian and shear-thinning droplets using the Droplet Rheology Classifier number (DRC) and Support Vector Machine (SVM) approach, respectively.

Table 2. Physical properties of fluids used for the study[39,40].

Liquid Type	$\boldsymbol{\rho_L}$ *(kg/m³)*	$\boldsymbol{\sigma L}$ *(mN/m)*	*N*	$\boldsymbol{\lambda}$ *(s)*	μ_o *(Pa. s)*	μ_∞ *(Pa. s)*	*Measured Contact angle over* $\boldsymbol{S_{PCG}}$
Water	998.5	72.2	-	-	0.001	0.001	----
Shear thinning (XG-1) (Xanthan Gum 0.052%)	1080	71.8	0.46	2.6	0.11	0.0036	111.5°
Newtonian ($\boldsymbol{\mu_\infty}$**)** (DI water with 40% glycerol, wt/wt)	1120.5	71	-	-	0.0036	0.0036	110.9°
Newtonian ($\boldsymbol{\mu_o}$**)** (DI water with 87% Glycerol, wt/wt)	1220	72	-	-	0.11	0.11	112.2°

2.2 Experimental setup and methodology

For the experimental study, the setup illustrated in Fig. 1(a) was used to record the static behaviour of the droplet. This experimental setup consists of a PDMS-coated glass slide mounted on a platform, whose inclination angle can be precisely adjusted using a mechanism consisting of two syringes connected by flexible tubing and mounted on a syringe pump. Two digital microscopes (Dino-Lite Edge 3.0 AM73915, UK) were used for recording the top and side views of the droplet placed over the S_{PCG} substrate. Droplets of different liquids of various volumes were placed over the substrate gently using variable volume micropipettes (Make: Tarsons) (refer to Fig. 1(a)). The recorded images of the side views of the droplet were then analysed using DinoCapture 2.0 and ImageJ software. To ensure reliable geometric measurements, all images were captured using a calibrated DinoLite digital microscope (2MP, 1280 × 960 pixels) with a spatial resolution of 1.157 µm/pixel. Measurements were performed manually at full zoom using ImageJ, and a conservative uncertainty of ±5 pixels (±5.79 µm) was considered for length scales. A detailed uncertainty analysis for the Bond number (≈ 0.58%) and DRC number (≈ 0.48%), including error propagation methodology, is provided in the Supplementary Material in section 2. All the experiments were repeated more than 5 times to ensure repeatability.

In the present work, the term equilibrium state or stable state refers to the pinned configuration of a droplet resting on the substrate. Such states are, in fact, metastable because the contact line is arrested by surface heterogeneities and contact angle hysteresis at the microscopic level, rather than representing the global minimum of surface free energy[41,42]. The droplet remains in this pinned state unless sufficient external energy is supplied to overcome the pinning barrier. Perturbations in the form of mechanical vibrations, substrate tapping, or sudden shocks can enable the contact line to depin and the droplet to relax into a new metastable configuration with altered base radius or contact angle. It should also be noted that under certain external excitations, droplets of both Newtonian and shear-thinning liquids may relax into comparable metastable states, in which their apparent shapes or measured macroscopic CAH values become similar despite differences in rheology (refer to fig. S4 in supplementary).

To further explore the influence of fluid rheology and deposition conditions, the spreading behaviour of Newtonian (μ_0), Newtonian (μ_∞), and shear-thinning (XG-1) droplets was recorded at 2871 FPS at (800 x 600) pixels resolution using a high-speed camera (Chronos 1.4, Kron Technologies) under three scenarios: (i) gentle deposition on a 30° inclined surface (impact velocity of 0.095m/s), (ii) gentle deposition on a horizontal surface (impact velocity of 0.095m/s) and (iii) droplet impact from a 5 cm height onto a horizontal surface (impact velocity of 0.7 m/s). Additionally, to study the effect of varying shear rates, the platform was inclined at different controlled rates, and the resulting deformation and macroscopic contact angle hysteresis (CAH) of the droplets were analysed to understand how shear rate influences droplet shape.

To determine the maximum retention force a substrate can apply onto a droplet, a droplet of known volume was placed on the substrate, and the volume of the droplet was gradually increased by adding 1.0 μL increments using a variable volume micropipette (Tarsons T10) (refer to Fig. 1(a)). The volume at which the droplet just begins to slide down the substrate was recorded as the maximum volume the substrate can retain. This volume indicates the point where gravitational force overcomes the retention force. The retentive force exerted by the substrate over the droplet was calculated using the mathematical model developed in our previous work (as shown in equation (1)) [24]. This model uses the droplet's geometry to calculate the retentive force. Here, the droplet geometry is fitted using a double-ellipse model for a droplet placed on an inclined substrate. The retentive force depends on the macroscopic contact angle hysteresis (or CAH) [14,15,24,43] and the contact area of the droplet.

$$F_s = \left[2\sigma_{la} r_1 \left\{CAH.K_r \left(-\frac{4}{\pi^2} + 0.5\right) - Cos\ \theta_R\right\} + 2\sigma_{la} r_2 \left\{CAH.\left(0.5 - \frac{4}{\pi^2}\right) + Cos\ \theta_F\right\}\right] - 2\sigma_{as}(r_2 - r_1) \quad (1)$$

In this work, we use macroscopic contact angles and contact angle hysteresis (CAH) for our analysis, as they provide a consistent and quantitative description of droplet shape and retention. The macroscopic contact angle was measured using the tangent-based method at the solid–liquid–vapor junction, which is robust, magnification-independent, and well suited for comparison. While microscopic interactions near the contact line affect local interface structure, the apparent macroscopic angle reflects the overall force balance that governs metastability, pinning, and retention. Hence, macroscopic CAH offers the most appropriate framework to describe retentive forces, metastability, and substrate interactions in our experiments[41,42,44].

2.3 Computational Classification: SVM

This work focuses on leveraging Support Vector Machines (SVMs) for accurate classification of Newtonian and non-Newtonian drops in a machine learning context. Support Vector Machines (SVMs) were implemented using scikit-learn, a popular Python library. This study aimed to differentiate these drop types based solely on their observable properties. It was hypothesized that by analysing features like macroscopic contact angle hysteresis, droplet volume, height, and length measured on an inclined substrate, an SVM model could be trained to effectively distinguish between Newtonian and non-Newtonian drops.

To achieve robust model performance, a meticulous data pre-processing pipeline was established. This pipeline addressed potential data quality issues that could hinder model learning. Missing values, which can introduce noise and bias, were eliminated using a list-wise deletion approach. Categorical variables were transformed into numerical representations through label encoding, enabling the SVM model to efficiently handle these features during the training process. 80% of the randomly chosen entries were chosen as training set, while 20% of the data were chosen for test set (dataset contained 93 entries). Additionally, feature scaling (standardization) was applied to ensure all features contributed equally during model training. Feature scaling is crucial for SVMs, as it places all features on a common scale, preventing features with larger ranges from dominating the model's decision-making process.

A critical aspect of our methodology involved optimizing the hyperparameters of the SVM model. An optimization technique, called grid search was employed to identify the optimal configuration for the model's parameters. This involved evaluating various combinations of hyperparameters, including the critical regularization parameter (C) and the kernel type. The regularization parameter (C) controls the trade-off between maximizing the margin that separates the classes and minimizing the misclassification error. The kernel type determines the way the model transforms the data into a higher-dimensional space, potentially allowing for more complex decision boundaries between the classes. The grid search determined that a linear SVM kernel with C set to 1 yielded the best performance on the test set. This optimized model achieved an accuracy of 95%, indicating its efficacy in distinguishing between Newtonian and non-Newtonian drops based on the chosen features.

Overall, this work demonstrates the potential of SVMs for accurate classification tasks, particularly in differentiating drop types based on measurable properties. The implemented data pre-processing pipeline and the optimized hyperparameter configuration through grid search were instrumental in achieving this success.

2.4 Statistics

Statistical analyses were conducted on two types of datasets: those obtained from repeated experiments on the same liquids, and those comparing result parameters between different liquids. As the data were not normally distributed, non-parametric methods were employed. A two-tailed Wilcoxon matched-pairs signed-rank test[45,46] was applied to evaluate differences between dependent datasets obtained under similar experimental conditions. A p-value less than 0.05 was considered statistically significant, indicating a meaningful difference between the datasets; otherwise, the datasets were interpreted as not significantly different.

3. Mathematical Analysis:

3.1 Shear stress variation along the droplet height

Here, we have derived a mathematical expression showing the variation in the shear stress along the droplet height for a static hemispherical droplet placed over inclined substrate [47]. This shear stress variation is important to realise the deformation in the droplet along its height.
Consider a droplet of hemispherical shape of radius R is resting on a substrate ABCD, inclined at an angle, δ. Consider an imaginary plane EFGH parallel to the substrate ABCD and cutting through the droplet at a height "a" from the bottom of the droplet (refer to Fig. 2(a)). Let the volume of the droplet above the droplet be upper volume, V_u and the volume below the cutting plane EFGH be the lower volume, V_L. Fig. 2(b) illustrates the cross-sectional view of the droplet layer along the EFGH plane, highlighting the force exerted on it due to the fluid volumes situated above the cross-sectional fluid layer.

$$Upper\ volume,\ V_U = \iiint_{z=a}^{z=R} \pi r^2 dz \tag{2}$$

$$V_U = \iiint_{z=a}^{R} \pi(R^2 - a^2) dz \tag{3}$$

Proceeding further with the integration, we get:

$$V_U = \pi \int_a^R (R^2 - z^2) dz = \pi \left[R^2 z - \frac{z^3}{3} \right]_a^R = \pi \left(R^3 - \frac{R^3}{3} - aR^2 - \frac{a^3}{3} \right) \tag{4}$$

On rearranging, the volume of the upper part of the hemispherical droplet is given by:

$$V_U = \pi \left[\frac{2R^3}{3} - aR^2 - \frac{a^3}{3} \right] \tag{5}$$

The Force at the dividing plane will be the gravity force over the plane due to the upper volume of the hemisphere,

$$F_s = \rho V_u g\ sin\delta \tag{6}$$

Which can be given as,

$$\tau = \rho \frac{V_u\, g \sin\delta}{A} \tag{7}$$

Where, A is the area of the circular cross section at height a

$$A = \pi R'^2 = \pi\,(R^2 - a^2) \tag{8}$$

Now, the shear stress at any height "a" along the hemispherical droplet can be given as,

$$\text{Shear stress: } \boldsymbol{\tau} = \frac{\rho\pi\left[\frac{2}{3}R^3 - aR^2 - \frac{a^3}{3}\right] g \sin\delta}{\pi(R^2 - a^2)} \quad ;\ \text{for } R > a > 0 \tag{9}$$

The equation (9) shows the variation in the shear stress along the droplet height for a hemispherical droplet placed on an inclined substrate. As clearly visible, the shear stress is directly proportional to the inclination angle θ, thus shear stress will increase with the increase in inclination angle for the same droplet at a fixed height location $'a'$. For Newtonian liquids, viscosity remains constant regardless of changes in shear stress. In contrast, shear-thinning liquids can exhibit a decrease in viscosity as shear stress increases, allowing the fluid to flow more easily under higher stress. To maintain analytical tractability, the shear stress model assumes a hemispherical droplet geometry and uniform power-law rheology. While actual droplets on inclined substrates may deviate slightly from hemisphericity, particularly under gravity-induced deformation, this approximation remains valid for the droplet volume range used in our experiments. Notably, the shear-thinning Xanthan Gum solution (XG-1) exhibits negligible elasticity [39,40], and the contact base remains nearly circular with a low height-to-width aspect ratio across tested inclinations. These observations support the applicability of the hemispherical assumption as a first-order model. Moreover, the consistency between the experimental trends and model predictions further justifies the use of this simplification for capturing dominant shear-thinning effects in the static regime.

When a shear-thinning droplet is gently deposited on an inclined surface, the gravitational component parallel to the substrate induces a transient shear stress within the droplet. Even though the droplet remains pinned and does not slide, internal fluid layers undergo deformation during the initial relaxation phase. This internal shear-induced deformation continues until the droplet attains mechanical equilibrium, resulting in a permanent alteration in droplet geometry and an increase in macroscopic contact angle hysteresis (CAH). The gravitational shear stress causing this deformation can be approximated as:

$$\tau \sim \rho g H sin\delta \tag{10}$$

where,

$$H = \frac{\pi\left(\frac{2}{3}R^3 - aR^2 - \frac{a^3}{3}\right)}{\pi(R^2 - a^2)} \tag{11}$$

For shear-thinning fluids, the viscosity decreases with increasing shear rate. The relationship between shear stress and shear rate can be approximated using a power-law form. It is important to note that the power-law model employed in this study does not capture the zero-shear viscosity plateau exhibited by more comprehensive rheological models such as the Carreau-Yasuda [48]. While this may introduce limitations at very low shear rates, the power-law model provides a simplified and analytically tractable framework to describe the dominant shear-dependent behaviour of the fluid within the scope of this scaling analysis. Moreover, rheological characterization of the shear-thinning fluid (XG-1) showed negligible elastic and time-dependent effects, justifying the use of a simplified viscous model.

$$\tau \sim k\dot{\gamma}^n \tag{12}$$

where, k is a constant, $\dot{\gamma}$ is the shear rate, and $n < 1$ is the power index for shear-thinning fluids. Balancing the above two equations for the induced shear rate:

$$\dot{\gamma} \sim \left(\frac{\rho g H sin\delta}{k}\right)^{\left(\frac{1}{n}\right)} \tag{13}$$

This induced shear rate leads to internal deformation, causing asymmetry at the contact line, which increases macroscopic CAH, even in the absence of droplet motion. In contrast, Newtonian fluids experience a more uniform and limited internal shear response under similar conditions, leading to a lower macroscopic CAH after equilibrium is reached.

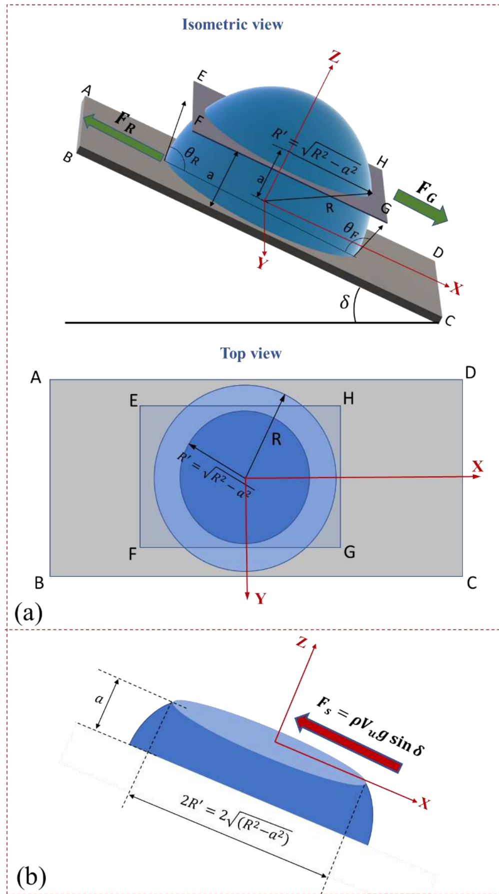

Fig. 2 (a) Isometric and top view of a static droplet over an inclined substrate (b) schematic showing force at the cut section of the droplet

3.2. Theoretical Scaling of the Droplet Rheology Classifier (DRC) with Bond Number

For a static pinned droplet resting on an inclined substrate, the gravitational force acting downslope is counterbalanced by the surface tension-induced retentive force resisting motion. This condition of equilibrium allows us to construct a theoretical scaling law that connects droplet geometry and interfacial forces with the Bond number (refer to top figure in Fig 2(a)).

$$F_g \approx F_R \tag{14}$$

$$F_g = \rho g V sin\delta \tag{15}$$

Since for a hemispherical droplet, $V = \frac{2}{3}\pi R^3$ (16)

$$F_g = \frac{2}{3}\pi \rho g R^3 sin\delta \tag{17}$$

$$Retentive\ Force, F_R = \gamma P(cos\theta_R - cos\theta_F) \tag{18}$$

For the small retained volume of droplet over S_{PCG}, the contact area perimeter can be reasonably approximated to be circular [49] and hence, perimeter can be written as

$$P = 2\pi R \tag{19}$$

$$Balancing\ the\ two\ forces, F_g \approx F_R \tag{20}$$

$$F_g = C\ F_R \tag{21}$$

where C is the scaling factor. Substituting F_g & F_R from equation 17 and 18 respectively into equation 21, we get:

$$\frac{2}{3}\pi\rho g R^3 \sin\delta = C.\gamma 2\pi R(cos\theta_R - cos\theta_F) \tag{22}$$

$$\frac{1}{3}\frac{\rho g R^2 sin\delta}{\gamma} = C.(cos\theta_R - cos\theta_F) \tag{23}$$

Substituting, $Bo = \frac{\rho g R^2}{\gamma}$,

$$Bo.sin\delta = 3.\mathrm{C}\,(cos\theta_R - cos\theta_F) \tag{24}$$

Here, $CAH = (cos\theta_R - cos\theta_F)$. Now, to systematically capture both droplet shape deformation and macroscopic contact angle hysteresis, we define the Droplet Rheology Classifier (DRC) number as:

$$DRC\ no. = \frac{\mathrm{H}}{\mathrm{L}}(\cos\theta_R - cos\theta_F) \tag{25}$$

Here, H and L represent the droplet height and base length, respectively. This dimensionless number quantifies asymmetry arising from internal rheological responses and geometric distortion under gravity,

Equation 25 can be rewritten as:

$$or, (cos\theta_R - cos\theta_F) = \frac{L}{H}DRC\ no. \tag{26}$$

Substituting in equation 24 we get,

$$Bo\ sin\delta = 3.C.\frac{L}{H}.DRC\ no. \tag{27}$$

This relation implies a linear dependence between Bo and DRC, where the slope encapsulates all physical and geometric scaling factors. To make it more generalized, we can rewrite it as:

$$Bo\ sin\delta = K_1.(L/H)DRC.no + K_2 \tag{28}$$

Here, the constants K_1 and K_2 represent the scaling slope and offset, respectively and will be determined using experimental data in the section 4.3.1. Equation 28, thus represents a mathematically derived relation between Bond number and the proposed DRC number. In the following sections (4.3.1), we will evaluate the utility of DRC no for classifying the droplets of Newtonian and shear thinning nature in different categories on DRC-Bo plot space.

4. Results and Discussion

4.1 Shear Stress Variation and Its effect on droplet deformation

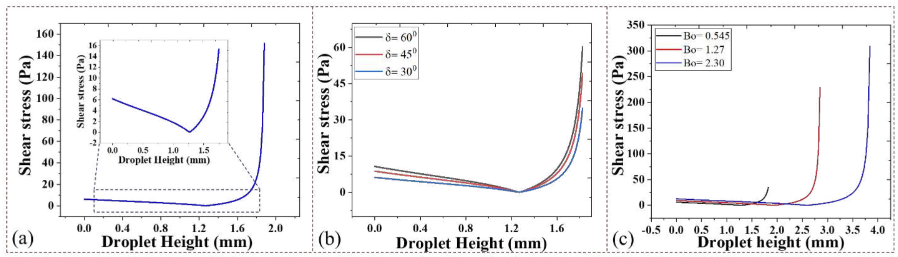

Fig. 3 (a) Variation in shear stress along the height of a hemispherical droplet of radius $R = 0.0019m$ placed on $30°$ inclined substrate (b) Variation in shear stress along the height of a hemispherical droplet of radius $R = 0.0019m$ at $30°, 45°$ and $60°$ inclination. (c) Influence of droplet size or Bond number on shear stress distribution.

As per the developed equation (9), the shear stress variation along the height of a static hemispherical droplet placed on an inclined substrate is illustrated in Fig. 3. Fig. 3(a) presents this variation for a droplet of radius 1.9 mm ($Bo = 0.545$) placed on a substrate inclined at 30°. The shear stress initially decreases along the height due to the reduction in the volume of fluid exerting downward force on each layer. However, beyond a certain height specifically 1.27 mm for a 1.9 mm radius droplet the cross-sectional area decreases significantly, causing a sharp rise in shear stress. At the base of the droplet, the shear stress is governed by the full droplet volume and maximum shear area, while at higher positions, the reduced volume above and narrower cross-section result in increased stress. This transition in stress profile correlates with the onset of greater droplet deformation.

Fig. 3(b) demonstrates the effect of varying inclination angles on shear stress distribution. It shows that increasing the inclination angle leads to a uniform rise in shear stress across the droplet's height due to the $(\sin\delta)$ dependence in the derived equation (10). This rise in shear stress enhances droplet deformation along height and thus results in macroscopic contact angle hysteresis. Although the droplet deforms under inclination, the position of the transition height where shear stress shifts from decreasing to increasing remains unaffected. This is because the transition height is governed solely by the droplet's geometry, particularly the internal relationship between the cross-sectional area at a given height and the volume of fluid above it. As a result, it is independent of inclination angle and instead determined by the droplet's base radius and height. In our observations, this transition consistently occurred at approximately 66% of the total droplet height, highlighting its geometry-driven nature.

Furthermore, Fig. 3(c) illustrates the influence of droplet size or Bond number on shear stress distribution. As the Bond number increases corresponding to larger droplet radii both the magnitude of shear stress and the transition height ($\approx 66\%$ $of\ total\ height$) increase. Additionally, the maximum shear stress within the droplet also rises with Bond number, indicating that larger droplets experience greater internal shear forces and more pronounced deformation under gravity.

4.2 Effect of droplet placement on the equilibrium shape of the droplet

4.2.1 Inclined Surface (impact velocity of 0.095m/s)

To investigate the behaviour of droplets of volume $10\mu L$ gently deposited on an inclined substrate, experiments were conducted on a PDMS-coated glass (S_{PCG}) surface inclined at 30°. The droplets impacted the surface with a very low velocity of 0.095 m/s (refer to the supplementary information on detailed methodology used for impact velocity measurement), corresponding to a negligible kinetic energy of approximately $45.04\ nJ$. Due to the droplet being on an inclined substrate, the gravitational tangential component introduced asymmetrical spreading, particularly in the downslope direction. The extent of this asymmetry varied with the rheological properties of the liquids. The highly viscous Newtonian(μ_0) fluid exhibited the largest spreading, resulting in the largest contact radius (refer to Fig. 4(a) and 4(b)). Its shear-independent viscosity allowed consistent flow under gravity, facilitating greater downslope deformation. In contrast, the shear thinning (XG-1) showed the least spreading. Despite a similar initial viscosity to Newtonian(μ_0) fluid, its apparent viscosity remained high under the low-shear conditions near the pinned contact line, resisting deformation. The lower-viscosity Newtonian (μ_∞) fluid exhibited an intermediate behaviour, with a contact radius between those of Newtonian(μ_0) and shear-thinning (XG-1). Rheological differences also affected CAH. Shear-thinning (XG-1) had the highest macroscopic CAH, indicative of strong pinning due to its shear-dependent viscosity. Newtonian (μ_∞) showed moderate macroscopic CAH, while the highly viscous Newtonian (μ_0) showed the lowest, owing to its stable, predictable response to gravitational stress, allowing smoother contact line relaxation (refer to Fig. 4(c)). It should be noted that the observed differences in final macroscopic CAH and droplet spread radius correspond to a metastable pinned state of the droplets, as discussed in the methodology section. These distinctions may change under external perturbations, where depinning could occur and droplets of different liquids may eventually relax into comparable shapes.

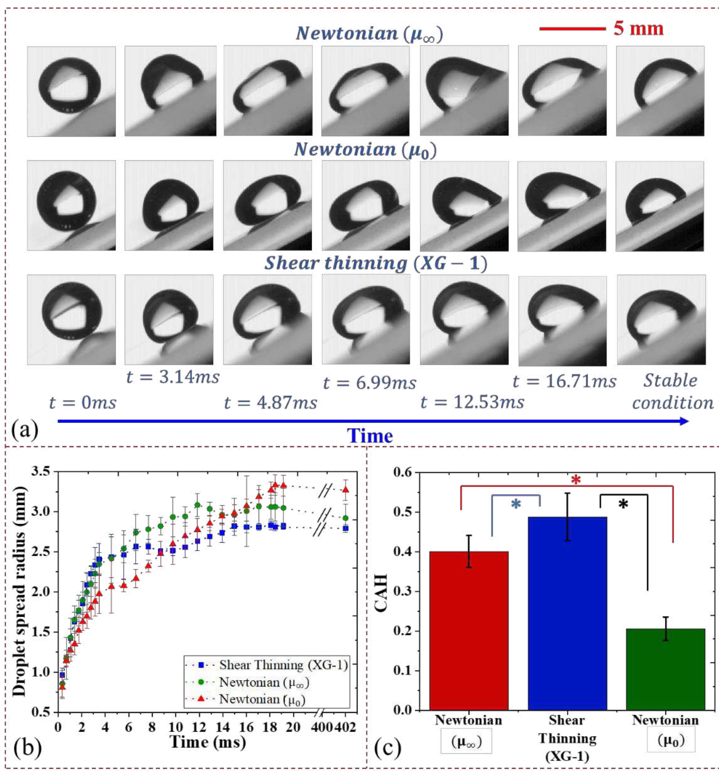

Fig. 4 (a) Droplet shape of different liquids at different time instants when dropped over an 30° inclined S_{PCG} with negligible impact velocity (0.095 m/s). (b) Variation in droplet spread radius with time while spreading over the substrate. (c) Macroscopic contact angle hysteresis for different liquid droplets after the droplet stabilises and obtains an equilibrium condition.

Statistical analysis: * indicates statistically significant differences ($p < 0.05$) between different fluid types determined by the Wilcoxon matched-pairs signed-rank test.

4.2.2 Horizontal Surface (impact velocity of 0.095m/s)

A similar experiment when repeated on a horizontal substrate, when droplets of volume $10\mu L$ were gently placed on a horizontal S_{PCG} surface with an impact velocity of 0.095m/s, spreading was primarily controlled by surface tension, viscosity, and adhesion. In the early stages, minor differences in spreading were observed, especially for the shear-thinning (XG-1) fluid, which exhibited lower viscosity under initial shear. However, in the absence of significant external forces, these differences diminished over time. Eventually, all three fluids reached equilibrium with nearly identical contact radii and contact angles (refer to Fig. S2 in the Supplementary material). At equilibrium, surface tension and adhesion dominated the shape, rendering rheological differences negligible.

4.2.3 Horizontal Surface (impact velocity of 0.7 m/s)

Droplets released from a height of 5 cm impacted the horizontal surface with an approximate velocity of 0.7 m/s, imparting a finite amount of kinetic energy ($\sim 2.44\ \mu J$) that introduced significant inertial effects during the spreading process. The final contact radii followed a similar trend as it was in the case of droplet deposition on an inclined substrate. The contact length was maximum for Newtonian (μ_0), followed by Newtonian (μ_∞) and the least for shear thinning (XG-1) (refer to Fig. S3 in Supplementary material).

The highly viscous Newtonian (μ_0) fluid dissipated impact energy steadily, spreading widely and reaching equilibrium quickly. The lower-viscosity Newtonian (μ_∞) spread rapidly but exhibited oscillations, leading to delayed stabilization and a slightly smaller final radius. The shear-thinning (XG-1) fluid initially spread quickly due to shear-induced viscosity reduction but later stiffened as shear decreased, limiting its final spread. These spreading behaviour are consistent with An et al. (2012)[27].

4.3 Geometrical Features of Shear-thinning and Newtonian liquid droplet: a comparison

Having established from previous experimental results that the equilibrium shape of a droplet is influenced by the method of placement, we now focus on analysing the equilibrium geometry of droplets gently deposited onto a substrate inclined at 30°. The geometrical characteristics of droplets at equilibrium were analysed for shear-thinning (XG-1) and Newtonian liquids placed on an inclined PDMS-coated glass (S_{PCG}) substrate. This comparison revealed distinct spreading and deformation behaviours between the two types of fluids. For droplets of equal volume ($2\ \mu L$), the Newtonian (μ_0) droplet exhibited a greater horizontal spread than the shear-thinning (XG-1) droplet, with a contact length that was 20.12% longer. Further, the Newtonian (μ_∞) droplet was 11.32% longer than the shear-thinning (XG-1) droplet (refer to Fig.5 (a) and (b)). On the other hand, the height of the shear-thinning (XG-1) droplet exceeded that of both Newtonian droplets. Specifically, the XG-1 droplet was 12.5% taller than the Newtonian (μ_0) droplet and 5.4% taller than the Newtonian (μ_∞) droplet (refer to Fig. 5 (a), and (c)). These observations suggest that the shear-thinning liquid spreads less and retains more vertical structure, indicating a greater resistance to deformation along the plane of the inclined surface. Such behaviour was consistent with earlier observations from spreading experiments conducted under negligible impact velocity (0.095 m/s) conditions on inclined substrates.

The higher vertical height and shorter base length of the shear-thinning droplets, coupled with increasing strain rate prior to attaining equilibrium state as moving along the height (Equation 13) make them more prone to tilting in the direction of motion, which contributes to increased macroscopic contact angle hysteresis (CAH). This is clearly illustrated in Fig. 5 (d) and 5(e), where the geometry of the shear-thinning droplet (with height H_2 and contact length L_2) contrasts with that of the Newtonian droplet (with height H_1 and contact length L_1). The observed increase in CAH for shear-thinning droplets is closely tied to their non-Newtonian nature. In such fluids, the viscosity is not uniform but varies with shear rate (refer to equation 13). Within the droplet, this results in different levels of shear deformation along its height, with greater deformation occurring along the height as shown in equation 13. This non-uniform deformation leads to higher asymmetry in the droplet shape, thereby enhancing the CAH. Experimental measurements confirmed that the macroscopic CAH of the XG-1 droplet was

23.28% higher than that of the Newtonian (μ_∞) droplet, and an even more pronounced 121.08% higher than that of the Newtonian (μ_0) droplet (refer to Fig. 5 (f)). Also, no significant variation in the macroscopic CAH was observed with thickness of PDMS coating on S_{PCG} as shown in Fig. 5(f), indicating that the mechanical response of the PDMS coating was constrained by the rigid glass support within the tested thickness range. Furthermore, statistical analysis performed on repeated measurements over the PDMS-coated glass (S_{PCG}) surface consistently yielded p-values greater than the chosen significance level (α), supporting the null hypothesis (Refer to Table S2 in supplementary). This indicates no statistically significant difference between repetitions and confirms the reliability and repeatability of the experimental measurements.

A two-tailed Wilcoxon matched-pairs signed-rank test was used to compare the experimental data. For each liquid, data from repeated trials (five repetitions per liquid) were compared pairwise (e.g., repetition 1–2, 1–3, 2–4, etc.), resulting in p-values greater than the significance threshold (α), as shown in Table S2 in the supplementary material. This indicates no statistically significant variation across repetitions, confirming the consistency of the experimental procedure for each liquid. In contrast, when comparing parameters such as droplet height, length, and macroscopic CAH between different liquids under identical conditions, the Wilcoxon test yielded p-values less than α. This indicates statistically significant differences, supporting the hypothesis that the equilibrium geometry of droplets can be used to distinguish between different liquids.

Further, the influence of droplet size and associated gravitational forces on macroscopic CAH was further explored by examining the effect of the Bond number ($Bo = \rho g R^2/\gamma$), particularly for smaller droplets ($Bo < 0.5$) when placed gently (impact velocity of 0.095m/s) over a S_{PCG} inclined at 30°, as shown in Fig. 5(g). The results indicated that for Bond numbers below 0.055, corresponding to very small droplets with volumes near 1 μL the macroscopic CAH remained nearly constant and minimal, suggesting negligible deformation (refer to Fig. 5(g)). However, once the Bond number exceeded 0.056, a clear increase in macroscopic CAH was observed for both Newtonian and shear-thinning droplets. This threshold behaviour implies that deformation due to gravity becomes significant only above a certain droplet size. Moreover, in this regime (Bo > 0.056), the shear-thinning droplets exhibited more substantial deformation than their Newtonian counterparts, reinforcing the conclusion that shear-thinning effects amplify deformation and hysteresis primarily at larger droplet volumes.

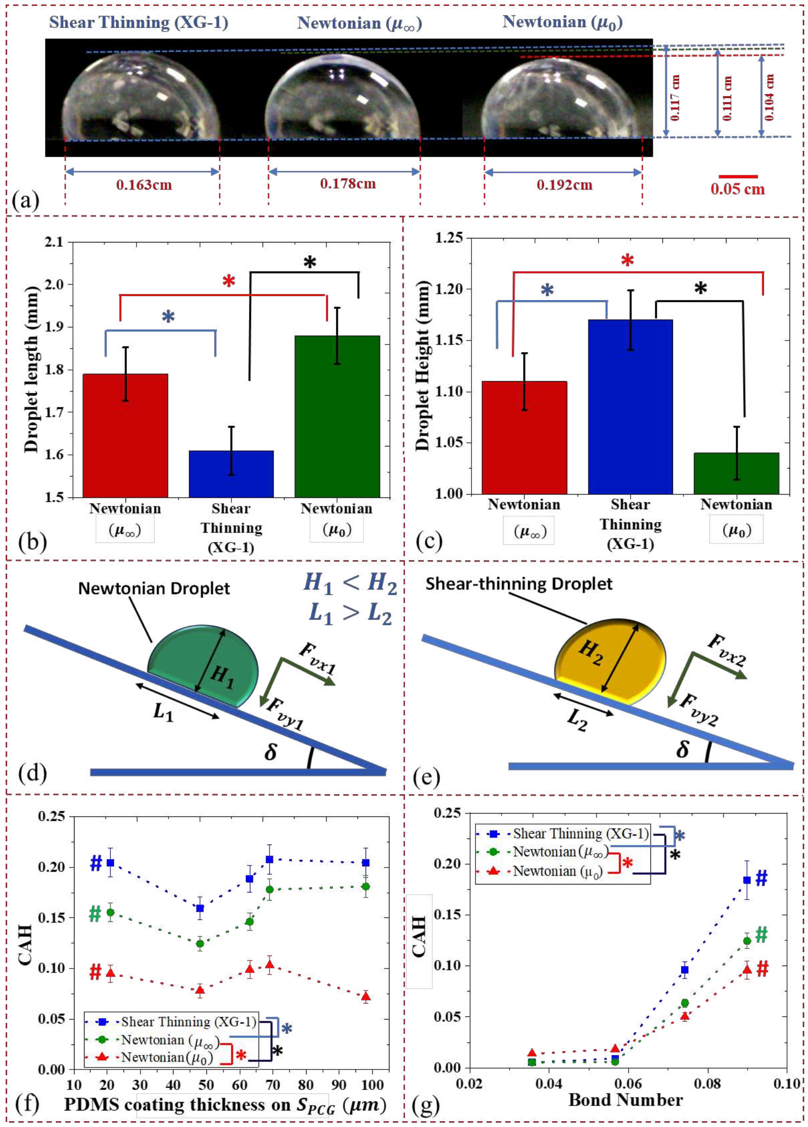

Fig. 5 **(a)** Height and length comparison between Newtonian and shear-thinning liquids for the same volume ($2\mu L$) over S_{PCG}. Here angle of inclination is 30°.**(b)** droplet length and **(c)** droplet height for droplets of the same volume (2 μL) of different liquids over PDMS-coated glass (S_{PCG}) inclined at 30°. Schematic showing the difference between height and contact length of droplets of the same volume of **(d)** Newtonian and **(e)** shear-thinning liquid over an inclined substrate. **(f)** Variation in macroscopic CAH of the same volume ($2\mu L$) of different liquids over varying thickness of PDMS coating over S_{PCG}. Variation with PDMS coating thickness on S_{PCG} is found to be insignificant with $p > 0.05$. **(g)** Variation in macroscopic CAH with bond number over S_{PCG} Inclined at 30° for different liquids.

Statistical analysis: * indicates statistically significant differences ($p < 0.05$) between different fluid types, while, # indicate no statistically significant difference across repeated measurements of the same fluid, as determined by the Wilcoxon matched-pairs signed-rank test.

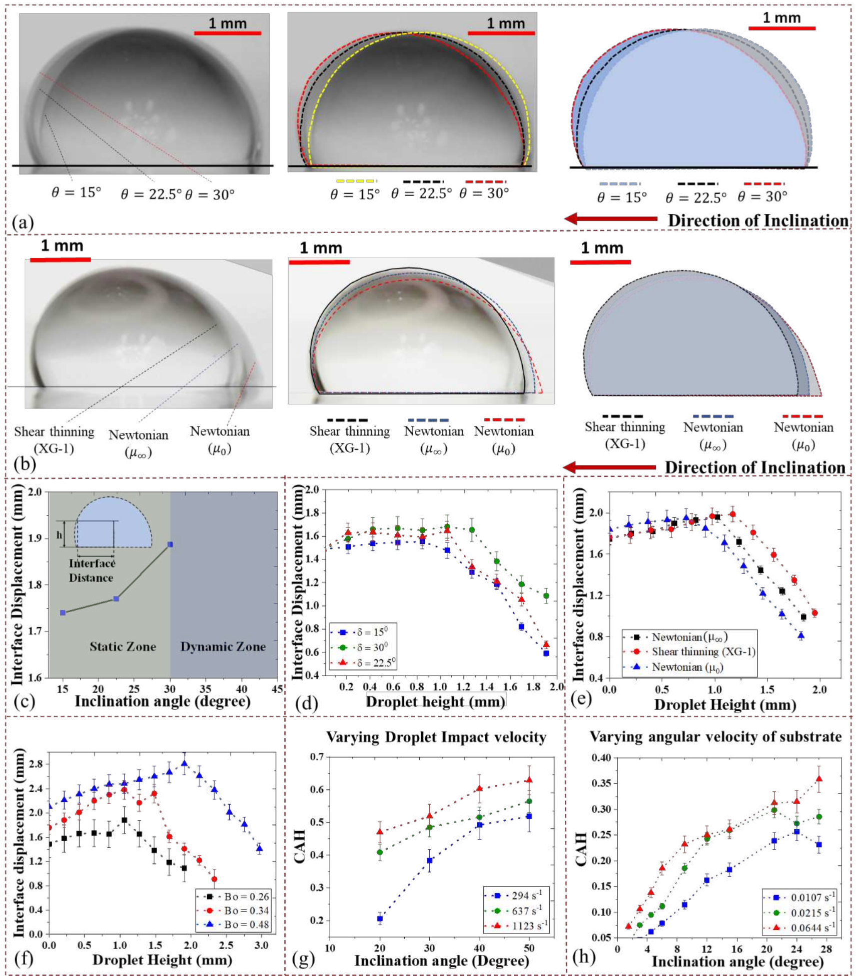

Fig 6: Change in shape of shear thinning (XG-1) droplet with respect to inclination angle, keeping the base radius the same. **(a)** overlapped images of the droplet, interfaces of the droplet traced and different interfaces of the droplet at different inclination angles. **(b)** Droplets of Shear thinning (XG-1), Newtonian (μ_0) and Newtonian (μ_∞) liquids of volume $15\mu L$ kept over S_{PCG}, inclined at 30, boundaries of the three overlapped droplets traced by dashed lines, and distinct shape of the three droplets. **(c)** Variation in interface distance with inclination angle of substrate. **(d)** Variation in interface displacement of Shear thinning (XG-1) droplet of volume $10\mu L$ for varying inclination angle **(e)** Variation in interface displacement of Newtonian and Shear thinning (XG-1) droplets of volume $10\mu L$ at 30° inclination. **(f)** Variation in interface displacement of Shear thinning (XG-1) droplets of varying Bond number at 30° inclination. **(g)** Variation in macroscopic CAH of droplet at equilibrium shape at

various inclination angle as a result of different shear rates due to different impact velocity **(h)** Variation in macroscopic CAH of Shear thinning (XG-1) droplet at equilibrium shape at various inclination angle with varying angular velocity of the substrate.

To further understand the effect of inclination on the deformation behaviour of shear-thinning droplets, experimental image analysis was carried out using side-view observations, as illustrated in Fig. 6 (a) and 6 (d). These figures present three shear-thinning (XG-1) droplets of equal volume ($15\ \mu L$) placed on the inclined S_{PCG} surface at different inclination angles of $15°, 22.5°, and\ 30°$ as shown in Fig. 6(a) and 6(d). The overlapping droplet images and the graph in Fig. 6 (d) clearly demonstrate that as the inclination increases, the bulk volume of the droplet shifts downward in the direction of gravity. This shift reflects a deformation along the droplet height, where the relative displacement between adjacent fluid layers increases progressively from the base toward the apex in agreement with equation (9) and equation (13).

To place these findings in perspective, a comparative analysis was conducted between the deformation behaviour of a shear-thinning droplet and that of Newtonian droplets under identical conditions. Fig. 6(b) shows side-view images of three droplets shear thinning (XG-1), Newtonian (μ_0), and Newtonian (μ_∞) each with a volume of $15\ \mu L$ and placed on the S_{PCG} surface inclined at 30°. The analysis of the deformation of interface from the images reveal that, just before the onset of motion, the Newtonian (μ_0) droplet exhibits the greatest spreading, followed by the Newtonian (μ_∞) droplet as shown in Fig 6(b) and 6 (e). In contrast, the shear-thinning (XG-1) droplet displays the least spreading. However, despite its smaller footprint, the shear-thinning (XG-1) droplet undergoes the most substantial internal deformation along its height (refer to Fig. 6(e)). This increased vertical distortion results in the highest macroscopic contact angle hysteresis and, therefore, the largest retentive force under static conditions.

The greater deformation observed in the shear-thinning (XG-1) droplet can be attributed to its non-Newtonian nature, where viscosity decreases with increasing shear rate. Since the shear stress intensifies along the droplet height with greater inclination, the local viscosity of the shear-thinning (XG-1) droplet is expected to drop in the upper layers, promoting further internal layer displacement. This rheological response distinguishes shear-thinning fluids from Newtonian ones, where viscosity remains constant and deformation is comparatively restrained.

This internal deformation is further driven by the increase in shear stress along the vertical axis of the droplet, as highlighted in Fig. 3(a). To quantify this deformation, the displacement of the droplet-air interface was tracked at a fixed height of 0.95 mm. As shown in the inset of Fig. 6(c), the position of the interface moves progressively farther from its initial location with increasing inclination, confirming that the deformation becomes more pronounced at steeper angles. This trend aligns well with the increase in shear stress as a function of inclination, illustrated in Fig. 3(a), Fig 6(c) and equation 13.

Such bulk deformation significantly influences the droplet's macroscopic contact angle hysteresis. As the inclination increases, the internal shear-driven deformation enhances the asymmetry between the front and rear contact angles, leading to a rise in macroscopic CAH. This relationship between deformation and macroscopic CAH continues until a critical inclination is reached. Beyond 30°, the droplet is no longer able to maintain a static state, and it transitions into motion. This transition is captured in Fig. 6(c), which distinguishes between the static and dynamic zones, marking the onset of droplet movement due to excessive deformation and gravitational force overcoming the retentive forces.

Furthermore, figure 6(f) presents the deformation of the droplet interface along its height for droplets with varying Bond numbers, showing clear agreement with the trends observed in Figure 3(c). It can be seen that the interface displacement becomes more pronounced with increasing Bond number, indicating that larger droplets experience stronger internal shear forces and greater gravitational deformation. Additionally, across all the cases discussed above, the transition in interface deformation is consistently observed at approximately 60% of the total droplet height, aligning with the theoretical prediction presented earlier in Figure 3 (transition height at approximately

66% of total height of the droplet). This consistent observation further strengthens the analytical framework and validates the geometry-governed nature of the deformation transition height.

Moreover, Fig. 6 (g) illustrates the variation in macroscopic CAH with inclination angle at different shear rates, where the shear rate refers to the maximum rate experienced at the droplet's contact line during spreading, induced by varying impact velocities. The results reveal that macroscopic CAH increases not only with shear rate but also with inclination angle at a fixed impact condition, suggesting that both gravitational forces and flow-induced shear synergistically enhance droplet deformation and contact line pinning.

Further insights into this behaviour were obtained through experiments involving varying inclination rates, which effectively changed the shear rate experienced by the droplet. As shown in Fig. 6(h), the macroscopic contact angle hysteresis of the shear-thinning (XG-1) droplet increased with increasing strain rate. A higher shear rate induces a more rapid reduction in viscosity within the droplet, which, combined with the vertical shear stress gradient, enhances the fluid's susceptibility to deformation. This leads to a progressive increase in macroscopic CAH with shear rate, further reinforcing the idea that the dynamic viscosity profile within shear-thinning droplets plays a critical role in governing their deformation and wetting behaviour on inclined hydrophobic substrates.

4.3.1 Comparison of Droplet Rheology Classifier (DRC) Number: A Unified Metric

As illustrated in Fig. 7, the DRC number effectively separates Newtonian and shear-thinning droplets into distinct zones across different Bond numbers. To assess the robustness and applicability of this metric, we conducted experiments with xanthan gum (XG) solutions at three different concentrations: 0.052% w/w, 0.128% w/w, and 0.153% w/w denoted as XG-1, XG-2, XG-3 respectively. The DRC values for all the three tested XG droplets remained significantly higher than those of the Newtonian droplets (with statistical significance $p < 0.05$ between different fluid types). This indicates that droplets with greater shear-thinning behaviour exhibit significantly higher DRC values, forming non-overlapping regions in the parameter space. This clear separation confirms that shear-thinning droplets tend to maintain more compact geometries and exhibit greater macroscopic contact angle hysteresis (CAH), both of which contribute to elevated DRC values.

Further, we also tested higher concentration of xanthan gum (0.258% w/w), when the fluid begins to exhibit viscoelastic behaviour rather than purely shear-thinning characteristics [39,40]. In this case, the DRC number could not distinctly separate the droplet behaviour from that of Newtonian fluids, indicating a breakdown in the classification. Thus, we can conclude the following. While the DRC number effectively captures the contrasting behaviours of shear-thinning and Newtonian droplets on inclined hydrophobic substrates, its formulation is specific to fluids exhibiting shear-thinning behaviour. For other non-Newtonian fluids, such as viscoelastic or yield-stress systems, additional parameters like elastic timescales or yield criteria may play a dominant role. Therefore, extending the DRC framework to these fluid classes may require incorporating appropriate other dimensionless numbers, such as the Deborah or Bingham number, to account for their additional elastic responses.

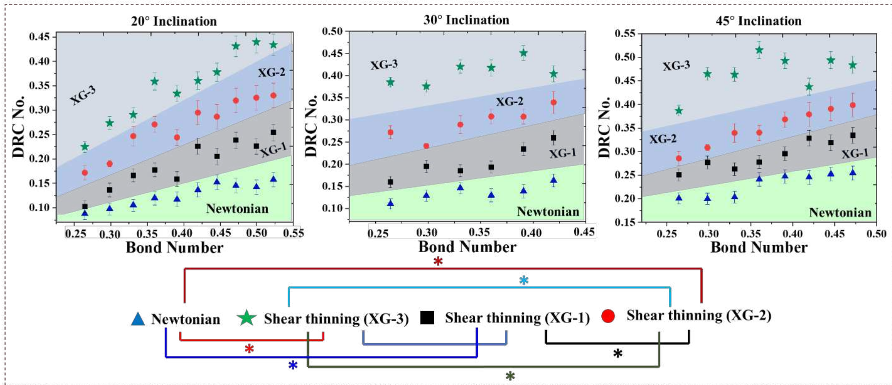

Fig. 7 Variation of Droplet Rheology Classifier (DRC) number (calculated using Equation (25)) with Bond number for Newtonian and shear-thinning droplets placed on inclined surfaces
Statistical analysis: * indicates statistically significant differences ($p < 0.05$) between different fluid types.

Further, the graph in Fig. 8(a) presents the empirically determined values of the constants K_1 and K_2 for Equation (28), obtained by fitting the experimental data to a linear relation (refer to Table S2 in the supplementary). The consistently positive slopes K_1 across all tested fluids and inclination angles reinforce a clear trend of Bond number increasing proportionally with DRC, confirming a robust physical correlation between droplet retention characteristics and gravitational forcing.

Additionally, the variation of K_1 across different fluid types and inclination angles reflects the DRC number's sensitivity to both rheological properties (e.g., Newtonian vs. shear-thinning behaviour) and substrate inclination. As illustrated in Fig. 8 (b-d), the theoretically predicted DRC numbers show distinct regimes for different fluids under varying Bond numbers and inclinations, aligning well with experimental observations.

This empirical and theoretical alignment supports the use of the DRC number as a discriminating metric. Newtonian and shear-thinning droplets exhibit clearly separated trends in the $DRC - Bo$ space, underscoring their differing deformation responses and macroscopic contact angle hysteresis behaviour. Therefore, the observed scaling relationships not only validate the physical basis of the DRC model but also establish it as a reliable and generalizable tool for classifying droplet dynamics across fluid types and experimental conditions such as varying inclination angle and varying droplet volume.

Further, for a small change in contact angle (<1°, θ_F= 97.438°, θ_R= 96.882°), the Bond number estimated using the relation ($Bo. \sin\delta = 3. C\ (cos\theta_R - cos\theta_F)$) yields a value of ~0.054 for an inclination angle of α = 30° and $C = 1$. This estimate aligns closely with the experimentally observed threshold value of Bo ≈ 0.056. Beyond this point, macroscopic contact angle hysteresis (CAH) begins to increase markedly, indicating a shift in the droplet's mechanical response to gravitational forces.

This behaviour signifies a transition from a geometry-preserving regime to a deformation-dominant regime, even though the contact line remains macroscopically pinned. At Bond numbers below ~0.056, macroscopic CAH remains low and changes minimally, suggesting limited internal deformation. However, beyond $Bo \approx 0.056$, the droplet begins to exhibit visible shape distortion, resulting in a substantial rise in macroscopic CAH. In this higher-Bo regime, the relationship between CAH and Bond number can be well-approximated by the same force-balance equation with a scaling constant $C \approx 0.12$, capturing the linear increase in CAH due to gravitational shear-induced deformation.

This sharp transition reflects the fact that droplet shape evolution does not require contact line motion. Instead, the pinned contact line allows redistribution of internal stress, enabling the droplet to deform asymmetrically while remaining stationary. Such behaviour has also been documented in previous studies which showed that pinned droplets can undergo considerable shape changes under increased inclination without depinning. These findings confirm that the observed macroscopic CAH increase beyond Bo ≈ 0.056 marks a mechanical deformation threshold, not a sliding onset, and can be effectively modelled using a consistent scaling law incorporating the empirically determined constant $C \approx 0.12$

Moreover, the graph plotted in Fig. 8(e) compares the theoretically calculated macroscopic CAH corresponding to different Bond number using the equation (24) with experimentally observed values of the CAH. The data show good agreement across the range, reinforcing the applicability of the model and validating the scaling approach.

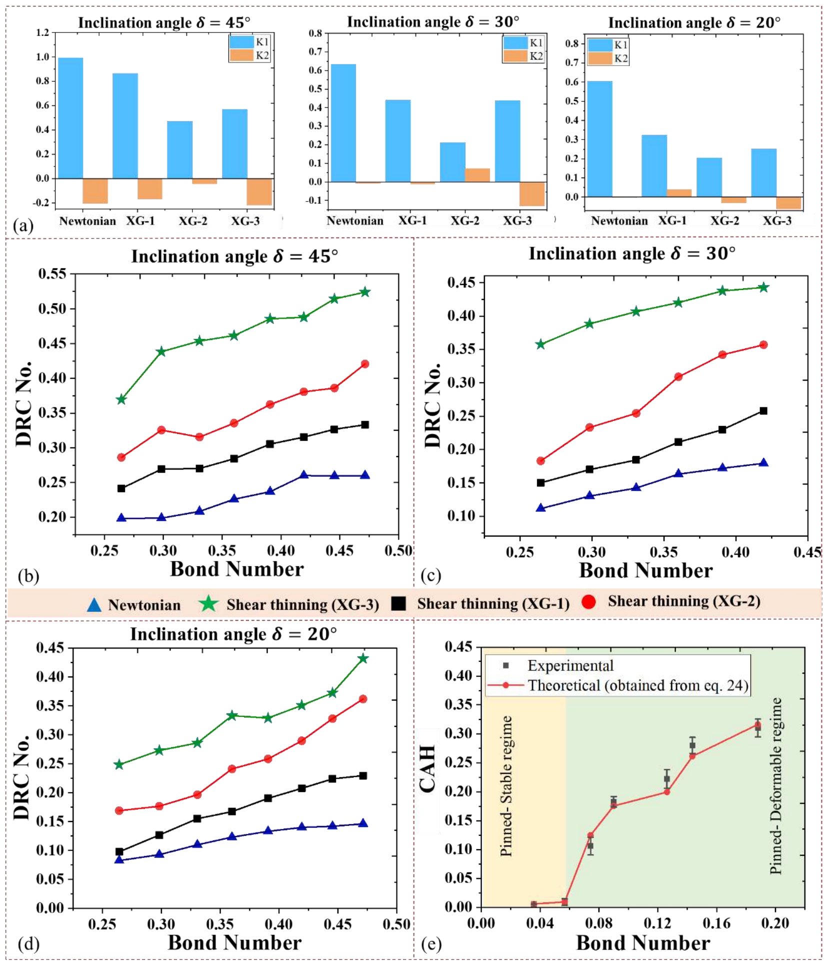

Fig 8: (a) values of the constants K_1 *and* K_2 for different liquids at different inclination angles. Theoretically predicted DRC numbers showing distinct regimes for inclination angle of (b) 45°, (c) 30° and (d) 20° (e) comparison of theoretically calculated Bond number with experimentally observed values for Shear thinning (XG-1) droplet. Here, $CAH = (cos\theta_R - cos\theta_F)$.

4.4 Retention behaviour of shear thinning and Newtonian liquid droplets

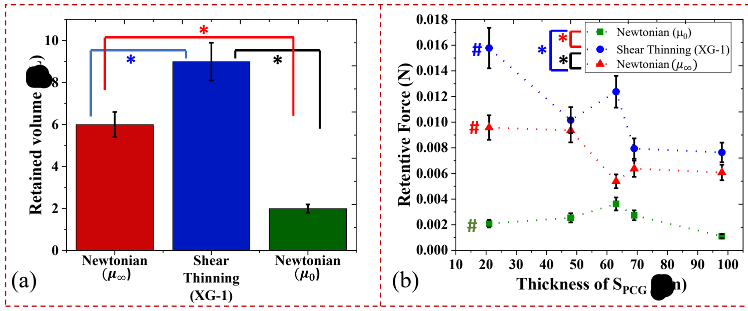

Fig. 9 (a) Retentive force by retained volume of different liquids over S_{PCG}. **(b)** Retentive force by retained volume of different liquids over S_{PCG}.
Statistical analysis: * indicates statistically significant differences ($p < 0.05$) between different fluid types, while # indicates no statistically significant difference across repeated measurements of the same fluid, as determined by the Wilcoxon matched-pairs signed-rank test.
Note: This plot shows the comparison of retentive force for Newtonian and shear-thinning liquid droplets calculated using equation 1.

As shown in Equation 1, the retentive force acting on a droplet is directly dependent on the macroscopic contact angle hysteresis (CAH). Based on our previous findings, shear-thinning liquids maintain a higher CAH in their equilibrium shape due to their shear-dependent viscosity, which induces significant bulk deformation during spreading and leads to stronger pinning forces.

To investigate this further, we conducted experiments to measure the retained volume of different liquids on the inclined PDMS-coated glass (S_{PCG}) substrate. As illustrated in Fig. 9(a), the shear-thinning liquid (XG-1) exhibited the highest retained volume, followed by the Newtonian (μ_∞) droplet, while the Newtonian (μ_0) droplet showed the least retention. Using the experimentally observed droplet geometry and applying Equation 1, we calculated the retentive force for each liquid. The results, shown in Fig. 9(b), indicate that the shear-thinning droplet exerted the maximum retentive force, consistent with its higher CAH and retained volume. Quantitatively, the retained volume of the shear-thinning (XG-1) droplet was approximately 50% higher than that of the Newtonian (μ_∞) droplet and nearly 350% greater than that of the Newtonian (μ_0) droplet. Also, no significant difference was observed in the retentive force with a change in the thickness of the S_{PCG}.

4.5 SVM-based classification of static droplet into Newtonian and Shear-thinning

Table 3: SVM Results for the given dataset

Metric	Newtonian	Non-Newtonian	Overall
Precision	0.88	1	-
Recall	1	0.92	-
F1-Score	0.93	0.96	-
Support	7	12	19
Accuracy	-	-	0.95

The support vector machine (SVM) achieved an overall accuracy of 95% on the test set, indicating it effectively distinguished between the two classes in the data, as shown in Table 3. While precision and recall are reported for each class separately, they generally show good performance Precision = (True Positives / (True Positives +

False Positives)), while Recall = True Positives / (True Positives + False Negatives). For Newtonian drops, the model achieved a precision of 0.88, meaning out of all data points predicted as Newtonian, 88% were actually Newtonian. Additionally, the recall of 1.0 for Newtonian drops suggests the model identified all actual Newtonian data points correctly. Similarly, non-Newtonian drops exhibit a high F1-score of 0.96, indicating a good balance between precision and recall for this class (where the F1 score is the harmonic mean of precision and recall). These results demonstrate that the SVM successfully learned patterns from the training data and effectively generalizes to unseen data in the test set.

To improve the statistical confidence in the performance metrics of the trained SVM classifier on a limited dataset (93 entries), we employed a bootstrapping approach over 1000 iterations. In each iteration, a bootstrap sample of the same size was drawn with replacement from the original data, and the model was trained on this resampled subset. Predictions were then made on the corresponding out-of-bag (OOB) samples those not selected in the given iteration. The classification accuracy for each OOB set was computed and aggregated across all iterations. This method allows us to estimate the variability of the model's performance and derive robust confidence intervals. The distribution of OOB accuracies over 1000 bootstrap runs is shown in Fig. 10 (a) (histogram), while the overall confusion matrix computed from all OOB predictions is illustrated in Fig. 10 (b). Additionally, the classifier's discriminative performance is assessed through the aggregated OOB-based ROC curve shown in Fig. 10 (c).

The statistical summary of the bootstrapped evaluation is presented in Table 4, including the mean OOB accuracy, standard deviation, and the 95% confidence interval (CI) estimated using the 2.5th and 97.5th percentiles of the accuracy distribution.

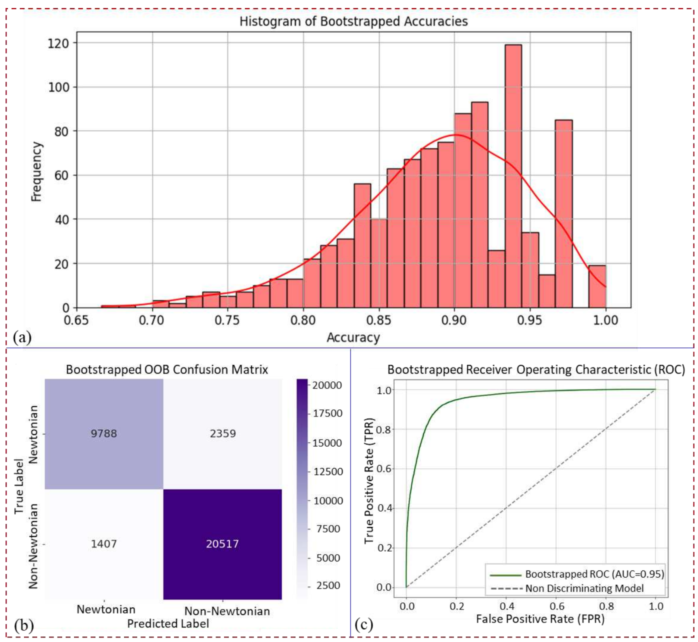

Fig 10: (a) Distribution of OOB classification accuracy from 1000 bootstrap runs. **(b)** Confusion matrix based on all OOB predictions. **(c)** ROC curve based on OOB predictions showing classifier performance.

Table 4: Summary of bootstrapped accuracy metrics based on OOB predictions (1000 iterations).

Metric	Value
Mean Accuracy	0.890107
Standard Deviation	0.058352
95% CI Lower	0.756588
95% CI Upper	0.973684

These results indicate a high and stable model performance, with relatively low variation across resampled data subsets. The bootstrapped 95% CI reinforces the model's reliability and generalization capability despite the limited dataset size.

Further, the performance of the model was evaluated on a new, unseen test dataset of Shear thinning XG-2 and XG-3 (0.128% w/w and 0.153 w/w) liquids. The model achieved a perfect accuracy of 1.0 on this new data. As shown in the classification report in Table 5, the model demonstrated a perfect performance for the "Non-Newtonian" class, achieving a precision, recall, and F1-score of 1.00. This indicates that the model correctly identified all instances of the Non- Newtonian class and had no false positives or false negatives on the new test data. The overall accuracy of 1.00 confirms the model's robust generalization ability.

Table 5: Classification performance of the trained model on unseen shear-thinning liquids (XG-2 and XG-3)

Model Accuracy on New Data: 1.000				
Classification Report on New data (Table Format)				
	Precision	**Recall**	**f1- score**	**Support**
Shear thinning	1.0	1.0	1.0	21.0
accuracy	1.0	1.0	1.0	1.0
Macro average	1.0	1.0	1.0	21.0
Weighted average	1.0	1.0	1.0	21.0

Further, the analysis in this study is based on a 0.052% w/w, 0.128% w/w and 0.153% w/w XG solution, chosen to exhibit shear-thinning behaviour with minimal viscoelasticity, enabling comparison with Newtonian reference fluids representing Newtonian (μ_0) and Newtonian (μ_∞). While this controlled contrast allows focused evaluation of the DRC and SVM framework, we acknowledge that XG rheology varies strongly with concentration. Future work should examine a broader concentration range including the viscoelastic effect of the liquid to test the robustness and scalability of the proposed classification scheme.

5 Conclusion

This study comprehensively examined the deformation behaviour, shear stress variation, and macroscopic contact angle hysteresis (CAH) of Newtonian and shear-thinning (XG-1) droplets on PDMS-coated surfaces under different conditions. Shear stress analysis revealed a non-linear variation along the droplet height, with a distinct increase near the top due to reduced cross-sectional area. This rising shear stress resulted in greater deformation along the droplet height, especially under inclined conditions. Experimental observations confirmed that XG-1 droplets deform more at steeper inclinations, correlating with increased shear stress, and leading to enhanced CAH and droplet displacement. Under static and impact conditions on horizontal surfaces, Newtonian (μ_0) droplets exhibited the greatest spreading due to gradual energy dissipation, whereas shear-thinning droplets spread less due to viscosity increase during deceleration. On inclined surfaces, Newtonian (μ_0) droplets again spread more, while shear-thinning (XG-1) droplets showed the highest CAH due to their shear-dependent viscosity, which restricts smooth contact line motion.

Geometrically, shear-thinning droplets exhibited up to 12.5% greater height and 20.12% shorter base length compared to Newtonian droplets, resulting in a more compact shape and higher tendency to tilt downslope, consistent with increased CAH. The deformation along height was negligible for Bond numbers <0.056, but significantly increased for $Bo > 0.056$, particularly in shear-thinning droplets. To unify these geometric and interfacial observations, a dimensionless parameter called the Droplet Rheology Classifier (DRC) number was introduced, defined as ($DRC = H/L\ (Cos\theta_R - Cos\theta_F)$), this metric effectively captures the combined influence of droplet aspect ratio and contact angle hysteresis. The DRC number demonstrated clear separation between Newtonian and shear-thinning droplets across varying Bond numbers, reinforcing its utility as a robust classifier of droplet rheology. It should be noted that all analyses in this work are based on the pinned configuration of the droplet, which represents a metastable rather than a true equilibrium state. Such states may change under external excitations, allowing Newtonian and shear-thinning droplets to relax into comparable configurations with similar macroscopic CAH despite differences in rheology. Our analysis is based on macroscopic contact angles measured by the tangent-based method, as these provide reliable, magnification-independent values that capture the global force balance governing droplet deformation, retention, and substrate interactions. It is also important to note that this study was conducted on a rigid PDMS-coated glass (S_{PCG}) substrate with negligible compliance. On significantly softer or viscoelastic substrates, such as soft gels, additional coupling between the droplet and substrate may arise due to factors like wetting ridge formation, enhanced contact line pinning, substrate deformation, and time-dependent viscoelastic relaxation. These effects can alter the apparent contact angle hysteresis (CAH), droplet asymmetry, and deformation behaviour, potentially affecting the geometric parameters and the DRC-based classification. While the conclusions drawn here remain valid for the rigid S_{PCG} substrate, future studies should explore these coupling effects to extend the applicability of the DRC framework to softer, more compliant systems.

The retentive force was found to be maximum for shear-thinning droplets, resulting in 50% and 350% higher retained volumes than Newtonian (μ_∞) and Newtonian (μ_0), respectively. This confirms stronger pinning and resistance to motion under inclined conditions.

A key advancement of this work lies in the successful classification of droplets using a Support Vector Machine (SVM) model. The model achieved 95% overall accuracy, with 0.88 precision and 1.0 recall for Newtonian droplets. For shear-thinning droplets, the F1-score was 0.96, highlighting a good balance between precision and recall. The ROC curve AUC of 0.96 and confusion matrix (100% accuracy for Newtonian, 92% for shear-thinning) demonstrate the model's robustness. Together, the experimental and machine learning results provide a strong framework for understanding and predicting complex droplet behaviour, emphasizing the importance of rheology in surface interactions. This classification method relies solely on visual inspection, eliminating the need for specialised equipment such as viscometers or rheometers, offering a simple and cost-effective approach for liquid categorisation into Newtonian and Shear-thinning.

Supplementary Material

Supplementary material document details the preparation, characterization, and experimental analysis of shear-thinning and Newtonian fluids used in the current study. Key components include:

- Fluid Preparation: Xanthan gum solution (shear-thinning) and glycerol-water mixtures (Newtonian) were prepared and matched for viscosity.
- Impact Velocity Measurement: High-speed imaging was used to calculate droplet impact velocities.
- Droplet Behavior Analysis: Droplet spreading and equilibrium shapes were studied at different impact velocities.
- Statistical Validation: Wilcoxon signed-rank tests confirmed repeatability and highlighted differences in droplet geometry and contact angle hysteresis between fluid types.

Conflicts of interest

The authors declare that they have no known conflicts of interest, whether financial or personal, that could be perceived as influencing the content of this paper.

Data Availability

The data that support the findings of this study are available from the corresponding author upon reasonable request.

Acknowledgments

The authors gratefully acknowledge the financial support provided by the Indian Council of Medical Research (ICMR) through grant no: 2022-18202/F1 and the Higher Education Financing Agency (HEFA) India through grant no: SAN/CSR/05/2022-23.

References

[1] P. Cooley, D. Wallace, B. Antohe, Applicatons of Ink-Jet Printing Technology to BioMEMS and Microfluidic Systems, Journal of the Association for Laboratory Automation 7 (2002) 33–39.
[2] J. Huang, Z. Yuan, S. Gao, J. Liao, M. Eslamian, Understanding Spray Coating Process: Visual Observation of Impingement of Multiple Droplets on a Substrate, J Shanghai Jiaotong Univ Sci 23 (2018) 97–105. https://doi.org/10.1007/s12204-018-1914-0.
[3] D. França, L.L. Messa, C.F. Souza, R. Faez, Nano and Microencapsulated Nutrients for Enhanced Efficiency Fertilizer, in: Polymers for Agri-Food Applications, Springer International Publishing, 2019: pp. 29–44. https://doi.org/10.1007/978-3-030-19416-1_3.
[4] L. Liang, X. Hu, Y. Shi, S. Zhao, Q. Hu, M. Liang, Y. Ai, Tunable and Dynamic Optofluidic Microlens Arrays Based on Droplets, Anal Chem 94 (2022) 14938–14946. https://doi.org/10.1021/acs.analchem.2c02437.
[5] F. Fontana, M.P.A. Ferreira, A. Correia, J. Hirvonen, H.A. Santos, Microfluidics as a cutting-edge technique for drug delivery applications, J Drug Deliv Sci Technol 34 (2016) 76–87. https://doi.org/10.1016/j.jddst.2016.01.010.
[6] V. Bertola, Some Applications of Controlled Drop Deposition on Solid Surfaces, 2008.
[7] B. Bin Wang, Y.P. Zhao, T. Yu, Fabrication of novel superhydrophobic surfaces and droplet bouncing behavior - Part 2: Water droplet impact experiment on superhydrophobic surfaces constructed using ZnO nanoparticles, J Adhes Sci Technol 25 (2011) 93–108. https://doi.org/10.1163/016942410X501115.
[8] J. Xie, J. Xu, W. Shang, K. Zhang, Mode selection between sliding and rolling for droplet on inclined surface: Effect of surface wettability, Int J Heat Mass Transf 122 (2018) 45–58. https://doi.org/10.1016/j.ijheatmasstransfer.2018.01.098.
[9] A. Mohammad Karim, H.P. Kavehpour, Spreading of emulsions on a solid substrate, in: J Coat Technol Res, Springer New York LLC, 2014: pp. 103–108. https://doi.org/10.1007/s11998-013-9510-6.
[10] B.S. Yilbas, G. Hassan, A. Al-Sharafi, H. Ali, N. Al-Aqeeli, A. Al-Sarkhi, Water Droplet Dynamics on a Hydrophobic Surface in Relation to the Self-Cleaning of Environmental Dust, Sci Rep 8 (2018) 1–19. https://doi.org/10.1038/s41598-018-21370-5.
[11] W. Meier, G. Greune, A. Meyboom, K.P. Hofmann, Surface tension and viscosity of surfactant from the resonance of an oscillating drop, n.d.
[12] A.I. ElSherbini, A.M. Jacobi, Retention forces and contact angles for critical liquid drops on non-horizontal surfaces, J Colloid Interface Sci 299 (2006) 841–849. https://doi.org/10.1016/j.jcis.2006.02.018.
[13] C.W. Extrand, Y. Kumagai, An Experimental Study of Contact Angle Hysteresis, J Colloid Interface Sci 191 (1997) 378–383.
[14] C.W. Extrand, Y. Kumagai, Liquid drops on an inclined plane: The relation between contact angles, drop shape and retentive force, Journal of Colloids and Interface Science (1994) 515–521.
[15] C.W. Extrand, A.N. Gent, Retention of Liquid Drops by Solid Surfaces, J Colloid Interface Sci 138 (1990) 431–442.
[16] C.G.L. Furmidge, Studies at phase interfaces 1. The sliding of liquid drops on solid surfaces and a theory for spray retention, J Colloid Sci 17 (1962) 309–324.
[17] R.P. Chhabra, Non-Newtonian Fluids: An Introduction, n.d.
[18] A.P. Deshpande, J.M. Krishnan, P.B.S. Kumar, Rheology of complex fluids, Springer New York, 2010. https://doi.org/10.1007/978-1-4419-6494-6.
[19] J. Milgram, M. Cheriet, R. Sabourin, R." Sabourin, "One Against One" or "One Against All": Which One is Better for Handwriting Recognition with SVMs?, n.d. https://inria.hal.science/inria-00103955.
[20] S.A. Haider, G. Kumar, T. Goyal, A. Raj, Stiffness estimation and classification of biological cells using constriction microchannel: poroelastic model and machine learning, Microfluid Nanofluidics 28 (2024). https://doi.org/10.1007/s10404-024-02710-6.
[21] P.J. Whitcomb, C.W. Macosko, Rheology of Xanthan Gum, J Rheol (N Y N Y) 22 (1978) 493–505. https://doi.org/10.1122/1.549485.
[22] E.L. Meyer, G.G. Fuller, R.C. Clark, W.-M. Kulicke, Investigation of Xanthan Gum Solution Behavior under Shear Flow Using Rheooptical Techniques, 1993. https://pubs.acs.org/sharingguidelines.
[23] Y. Sun, Z. Wei, J. Zhou, A. Mao, D. Bian, Modification of magnetorheological fluid and its compatibility with metal skeleton: Insights from multi-body dissipative particle dynamics simulations and experimental study, Physics of Fluids 36 (2024). https://doi.org/10.1063/5.0190978.
[24] S.A. Haider, Rohit, A. Raj, Retention analysis of droplets over compliant substrates, Colloids Surf A Physicochem Eng Asp 673 (2023). https://doi.org/10.1016/j.colsurfa.2023.131800.
[25] A.I. ElSherbini, A.M. Jacobi, Liquid drops on vertical and inclined surfaces: I. An experimental study of drop geometry, J Colloid Interface Sci 273 (2004) 556–565. https://doi.org/10.1016/j.jcis.2003.12.067.
[26] G. Macdougall, I. The adhesion of liquids to solids and a new method of determining the surface tension of liquids, n.d. https://royalsocietypublishing.org/.

[27] S.M. An, S.Y. Lee, Observation of the spreading and receding behavior of a shear-thinning liquid drop impacting on dry solid surfaces, Exp Therm Fluid Sci 37 (2012) 37–45. https://doi.org/10.1016/j.expthermflusci.2011.09.018.
[28] V.M. Starov, A.N. Tyatyushkin, M.G. Velarde, S.A. Zhdanov, Spreading of non-Newtonian liquids over solid substrates, 2003. www.elsevier.com/locate/jcis.
[29] X.D. Wang, Y. Zhang, D.J. Lee, X.F. Peng, Spreading of completely wetting or partially wetting power-law fluid on solid surface, Langmuir 23 (2007) 9258–9262. https://doi.org/10.1021/la700232y.
[30] S. Rafaï, D. Bonn, A. Boudaoud, Spreading of non-Newtonian fluids on hydrophilic surfaces, J Fluid Mech 513 (2004) 77–85. https://doi.org/10.1017/S0022112004000278.
[31] S. Varagnolo, G. Mistura, M. Pierno, M. Sbragaglia, Sliding droplets of Xanthan solutions: A joint experimental and numerical study, European Physical Journal E 38 (2015) 1–8. https://doi.org/10.1140/epje/i2015-15126-0.
[32] E. Nader, S. Skinner, M. Romana, R. Fort, N. Lemonne, N. Guillot, A. Gauthier, S. Antoine-Jonville, C. Renoux, M.D. Hardy-Dessources, E. Stauffer, P. Joly, Y. Bertrand, P. Connes, Blood rheology: Key parameters, impact on blood flow, role in sickle cell disease and effects of exercise, Front Physiol 10 (2019). https://doi.org/10.3389/fphys.2019.01329.
[33] C. Lapouméroulie, P. Connes, S. El Hoss, R. Hierso, K. Charlot, N. Lemonne, J. Elion, C. Le Van Kim, M. Romana, M.-D. Hardy-Dessources, New insights into red cell rheology and adhesion in patients with sickle cell anaemia during vaso-occlusive crises, Br J Haematol 185 (2019). https://doi.org/10.1111/bjh.15686ï.
[34] G.B. Proctor, A.M. Shaalan, Disease-Induced Changes in Salivary Gland Function and the Composition of Saliva, J Dent Res 100 (2021) 1201–1209. https://doi.org/10.1177/00220345211004842.
[35] J.T. Ma, C. Tang, L. Kang, J.A. Voynow, B.K. Rubin, Cystic Fibrosis Sputum Rheology Correlates With Both Acute and Longitudinal Changes in Lung Function, Chest 154 (2018) 370–377. https://doi.org/10.1016/j.chest.2018.03.005.
[36] E.B.V. Dussan, On the ability of drops or bubbles to stick to non-horizontal surfaces of solids. Part 2. Small drops or bubbles having contact angles of arbitrary size, J Fluid Mech 151 (1985) 1–20. https://doi.org/10.1017/S0022112085000842.
[37] V. Berejnov, R.E. Thorne, Effect of transient pinning on stability of drops sitting on an inclined plane, Phys Rev E Stat Nonlin Soft Matter Phys 75 (2007). https://doi.org/10.1103/PhysRevE.75.066308.
[38] G. Ahmed, M. Sellier, Y.C. Lee, M. Jermy, M. Taylor, Modeling the spreading and sliding of power-law droplets, Colloids Surf A Physicochem Eng Asp 432 (2013) 2–7. https://doi.org/10.1016/j.colsurfa.2013.05.015.
[39] M.T. Islam, A. V. Nguyen, A. Afzal, Bubble's rise characteristics in shear-thinning xanthan gum solution: a numerical analysis, J Taiwan Inst Chem Eng 132 (2022). https://doi.org/10.1016/j.jtice.2022.104219.
[40] S. Amirnia, J.R. De Bruyn, Maurice.A. Bergougnou, A. Margaritis, Continuous rise velocity of air bubbles in non-Newtonian biopolymer solutions, Chemical Engineering Sciences 94 (2013) 60–68.
[41] E.L. Decker, B. Frank, Y. Suo, S. Garoff, Physics of contact angle measurement, 1999. www.elsevier.nl/locate/colsurfa.
[42] H. Zhang, H. Zhang, F. Wang, B. Nestler, Exploration of contact angle hysteresis mechanisms: From microscopic to macroscopic, Journal of Chemical Physics 161 (2024). https://doi.org/10.1063/5.0232287.
[43] E. Pierce, F.J. Carmona, A. Amirfazli, Understanding of sliding and contact angle results in tilted plate experiments, Colloids Surf A Physicochem Eng Asp 323 (2008) 73–82. https://doi.org/10.1016/j.colsurfa.2007.09.032.
[44] E. Ramé, S. Garoff, Microscopic and Macroscopic Dynamic Interface Shapes and the Interpretation of Dynamic Contact Angles, 1996.
[45] A. Damerau, M. Kirchner, P. Mertins, F. Buttgereit, T. Gaber, A point-of-research decision in synovial tissue engineering: Mesenchymal stromal cells, tissue derived fibroblast or CTGF-mediated mesenchymal-to-fibroblast transition, Eur J Cell Biol (2024) 151455. https://doi.org/10.1016/j.ejcb.2024.151455.
[46] B. Rosner, R.J. Glynn, M.L.T. Lee, The Wilcoxon signed rank test for paired comparisons of clustered data, Biometrics 62 (2006) 185–192. https://doi.org/10.1111/j.1541-0420.2005.00389.x.
[47] A. Khaldoun, P. Moller, A. Fall, G. Wegdam, B. De Leeuw, Y. Méheust, J. Otto Fossum, D. Bonn, Quick Clay and Landslides of Clayey Soils, Phys Rev Lett 103 (2009). https://doi.org/10.1103/PhysRevLett.103.188301.
[48] K.Y. Pérez-Salas, E.L. García-Romero, A.A. Barrientos-Cruz, S. Sánchez, G. Ascanio, J.P. Aguayo, Elastic and shear-thinning effects in contraction flows: a comparison, Rheol Acta 63 (2024) 585–601. https://doi.org/10.1007/s00397-024-01462-y.
[49] T.W.G. Van Der Heijden, A.A. Darhuber, P. Van Der Schoot, Macroscopic Model for Sessile Droplet Evaporation on a Flat Surface, Langmuir 34 (2018) 12471–12481. https://doi.org/10.1021/acs.langmuir.8b02374.